Check for updates

Experimental and theoretical investigations of the effect of heteroatom-doped carbon microsphere supports on the stability and storage capacity of nano-Co_3O_4 conversion anodes for application in lithium-ion batteries†

Pravin K. Dwivedi,[ab] Aathira Nair,[a] Rupali S. Mehare,[ab] Vikash Chaturvedi,[ab] Kavita Joshi [ID] *[ab] and Manjusha V. Shelke [ID] *[ab]

Conversion-type anode materials have been intensely studied for application in Li-ion batteries (LIBs) due to their potentially higher capacities than current graphite-based anodes. This work reports the development of a high-capacity and stable anode from a nanocomposite of N and S co-doped carbon spheres (NSCSs) with Co_3O_4 (NSCS–Co_3O_4). A hydrothermal reaction of saccharose with L-cysteine was carried out, followed by its carbonization. CSs when used as supports for conversion-type materials provide efficient electron/ion transfer channels, enhancing the overall electrochemical performance of the electrodes. Additionally, the heteroatoms doped in a carbon matrix alter the electronic properties, often increasing the reactivity of the carbon surface, and they are reported to be effective for anchoring metal oxide nanoparticles. Consequently, the NSCS–Co_3O_4 nanocomposites developed in this work exhibit enhanced and stable reversible specific capacity over several cycles. Stable cycling behavior was observed at 1 A g^{-1} with 1285 mA h g^{-1} of specific capacity retained after 350 cycles along with more than 99% of coulombic efficiency. This material shows excellent rate capability with a specific capacity of 745 mA h g^{-1} retained even at a high current density of 5 A g^{-1}. Detailed DFT-based calculations revealed the role of doped supports in controlling the volume expansion upon lithiation.

Introduction

LIBs are one of the most studied systems for clean energy storage due to their compact size, longer life cycle, high efficiency and high energy density.[1,2] Their ever-increasing demand for the extended range of advanced applications, *e.g.*, electric mobility requires high energy and high power densities.[3–5] Since decades, intense research has been done on transition metal oxides such as CoO, MnO_2, Fe_2O_3, and Co_3O_4 to replace graphitic anodes that have a limited theoretical capacity of 372 mA h g^{-1} *vs.* Li$^+$.[6–8] Among them, Co_3O_4 can be produced in large volumes due to its low cost, and it has been demonstrated as a potential high-energy material for application in LIBs with a theoretical capacity of around 890 mA h g^{-1}.[9] However, the commercial application of Co_3O_4 has not been viable yet due to its low electrical conductivity, high volume expansion during charge and discharge cycles, capacity fading at high current

density, and poor cyclic stability.[10,11] Some new synthesis strategies have been demonstrated for producing nanostructures of Co_3O_4 with different morphologies having different pore distributions and a specific surface area, leading to the high capacity and improved stability of LIBs.[12–19] The high surface areas and small dimensions of these nanostructures help to improve the interaction of the electrode–electrolyte surface and reduce the Li-ion diffusion length into the solid surface. However, the high volume expansion of Co_3O_4 results in the crystal deformation and agglomeration of anode materials, restricting the capacity gains.[20] It has been reported that preparing composites of metal oxide nanostructures with conducting carbon networks compensates for the volume expansion and the lacking conductivity, which also enhances the electrochemical performance. This strategy helps in remarkably reducing the volume expansion of Co_3O_4; moreover, the carbon matrix improves the conduction of electrons to the current collector.[21] Different carbon forms such as nano-onions, nanotubes, nanofibers, graphene sheets and 3D porous carbon networks are widely used to prepare composites with Co_3O_4, demonstrating anodic capacity enhancement.[21–28] Among these carbon structures, spherical carbon has maximum packing density, low surface-to-volume ratio and high structural

[a]Physical and Materials Chemistry Division, CSIR-National Chemical Laboratory, Pune 411008, MH, India. E-mail: mv.shelke@ncl.res.in; k.joshi@ncl.res.in

[b]Academy of Scientific and Innovative Research (AcSIR), Ghaziabad-200112, UP, India
† Electronic supplementary information (ESI) available. See DOI: 10.1039/d0na00261e

resistance.[29–31] However, there is a large scope for further improvements in the performance by introducing defects in carbon matrices, *e.g.*, doping of heteroatoms such as N, B, and S.[32–37] These dopant atoms on the surface of carbon materials improve the reactivity, which enhances the lithiation capacity. Additionally, the large atomic size of sulfur atoms can increase the interlayer spacing of the graphitized carbon, create micropores in the carbon matrix and hence improve the charge storage capacity of the carbon material. Moreover, lone-pair electrons of N and S atoms contribute to extending the conjugated electron clouds of the carbon matrix, resulting in increased conductivity that enhances the rate capacity and cycle life of the electrode material.

Taking into consideration the potential effects of the co-doped carbon matrix for the stable performance of high-energy conversion-type anode materials like metal oxides, we synthesized a composite of nitrogen and sulphur co-doped carbon spheres and Co_3O_4 as an anode material for application in LIBs with enhanced reversible capacity and potential for large-scale production (Scheme 1). N and S co-doping in carbon spheres is found to efficiently inhibit the agglomeration of Co_3O_4 NPs and facilitate robust interactions between the electrode and Li-ions, which improves the kinetics of lithium diffusion and reduces the charge transfer resistance. The NSCS–Co_3O_4 nanocomposite exhibits excellent rate performance with a specific capacity of 745 mA h g^{-1} at a high current density of 5 A g^{-1}. It retains a remarkable and stable discharge capacity of 1285 mA h g^{-1} at 1 A g^{-1} after 350 cycles with more than 99% coulombic efficiency.

Experimental section

Synthesis of NS co-doped carbon spheres

For the synthesis of NS co-doped carbon spheres, saccharose and L-cysteine in 5 : 1 ratio were used as precursors. In a typical experiment, 10 g of saccharose was first dissolved in 120 ml of de-ionized water followed by the addition of 2 g of L-cysteine

Scheme 1 Schematic of the synthesis of the NSCS–Co_3O_4 nanocomposite.

under stirring. The resultant solution was then treated hydrothermally at 180 °C for 24 h. After cooling down to room temperature, the obtained product was washed several times with de-ionized water and ethanol by vacuum filtration followed by overnight drying at 80 °C. After drying, the as-prepared material was annealed at 800 °C in an inert atmosphere for 1 h. For the synthesis of non-doped CSs, only saccharose was treated hydrothermally.

Synthesis of a Co_3O_4 NP composite with NS co-doped carbon spheres
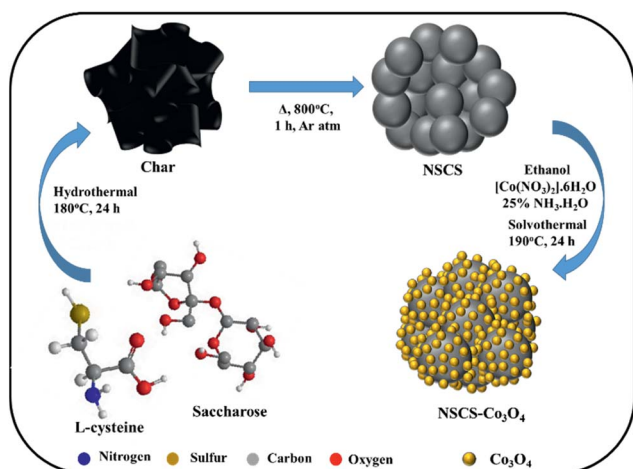
To synthesize an NSCS–Co_3O_4 nanocomposite, 50 mg of NSCS was dispersed in 20 ml of ethanol by ultra-sonication and a separate solution of 0.29 g of $Co(NO_3)_2 \cdot 6H_2O$ in 20 ml of ethanol was prepared by stirring. Both solutions were mixed under stirring for 30 minutes followed by the addition of ammonia solution ($NH_3 \cdot H_2O$, 25%). The obtained solution was then transferred into a Teflon-lined stainless steel autoclave and heated at 190 °C for 24 h. Finally, the reaction mixture was washed with DI water and ethanol by vacuum filtration followed by overnight drying at 80 °C. For comparison, pure Co_3O_4 was synthesized without the addition of NSCSs and CS–Co_3O_4 with non-doped CSs.

Material characterization

Powder X-ray diffraction (p-XRD) patterns were recorded using a Phillips PAN analytical diffractometer with CuKα radiation (λ = 1.5406 Å). Transmission electron microscopy (TEM) was carried out using a Tecnai F30 FEG machine operating at an accelerating voltage of 300 kV. The morphology and chemical composition of the ternary hybrid composite were examined using a Quanta 200 3D, FEI scanning electron microscope (SEM). X-ray photoelectron spectroscopic (XPS) measurements were carried out using a VG Micro Tech ESCA 3000 instrument. Thermogravimetric analysis (TGA) was performed using an SDT model Q600 of TA instrument at a heating rate of 10 °C min^{-1} in an air atmosphere.

Electrochemical characterization

The electrochemical properties of the as-prepared electrode materials were examined in a two-electrode coin cell (CR2032) configuration. The Co_3O_4 nanostructures, non-doped CSs and NSCS–Co_3O_4 were tested as anode materials by preparing their slurry with a conducting carbon additive (super P) and a binder (polyvinylidene difluoride, PVDF) in an NMP solvent. Further, the slurry was coated onto a Cu foil, which serves as the current collector, and subsequently dried at 90 °C overnight before assembling the cell in an Ar-filled glove box. The average mass loading of the active material in various electrodes was nearly 1 mg. The coin cells were assembled using a lithium metal foil as the counter electrode, a quartz microfiber paper (Whatman) as the separator and 1 M LiPF$_6$ in ethylene carbonate (EC)–diethyl carbonate (DEC) (1 : 1 by volume) as the electrolyte. Cyclic voltammetry (CV) was performed using a SP-300 EC Biologic potentiostat at a scan rate of 0.25 mV s^{-1} in the potential window of 0.01–3.0 V. The galvanostatic discharge–

charge cycling of the cells was carried out at different current densities between the potential windows of 0.01 V and 3.0 V using an MTI battery analyser. The electrochemical impedance spectroscopy (EIS) spectra were used to measure the impedance in the frequency range from 100 kHz to 50 mHz with an AC amplitude of 10 mV.

Computational details

All the calculations were carried out using the Kohn–Sham formulation of DFT. The projector augmented wave potential[38] is used with the Perdew–Burke–Ernzerhof (PBE) approximation for the exchange-correlation[39] and generalized gradient approximation, as implemented in a plane-wave, pseudo-potential-based code, VASP.[40–42] Furthermore, for the correct representation of 3d orbitals of Co, spin-polarized calculations with the Hubbard U correction (GGA + U) were included. The U parameter (3.32 eV) was selected from the material project[43] and further verified for its transferability. The Monkhorst–Pack (MP) formulation was used for the grid of $6 \times 6 \times 6$, for bulk Co_3O_4, which resulted in 108 k-points in the irreducible Brillouin zone (IBZ) and yielded an energy convergence of about 0.005 eV. While, for the composites of Co_3O_4 with doped and undoped graphite, a 2D slab was created with a vacuum of 15 Å, which increased appropriately as lithiation progressed. A gamma-centered grid of $6 \times 6 \times 1$ was employed for all the surface calculations. This choice of MP grid resulted in 20 k-points in the IBZ. As Li-ions are alloying with Co_3O_4 and its composites, the enthalpy of alloy formation ΔE_{mix} is calculated (see eqn (1)) to estimate the stability of the systems:[44]

$$\Delta E_{mix} = E_{sys} - \text{Ratio}_{sys} \times E_{Li} - (1 - \text{Ratio}_{sys}) \times E_{bare\_sys} \quad (1)$$

where E_{bare_sys}, E_{Li} and E_{sys} are the energy of the bare systems (Co_3O_4, CS–Co_3O_4, and $NSCS$–Co_3O_4), Li atom, and Li alloyed systems respectively. The Ratio$_{sys}$ is taken as the ratio of the number of alloyed Li atoms to the total number of the atoms in the system. We modelled the charging of the electrode via the lithiation process by varying the number of Li atoms from 0 to 64 in steps of 8. To model CS–Co_3O_4 and $NSCS$–Co_3O_4 systems, the periodic 2D slab was used by layering Co_3O_4 on undoped and doped graphite. Sufficient vacuum was added to minimize the interaction between the subsequent periodic images. Furthermore, the bottom two layers of graphite were fixed to represent the bulk of the system and all other layers were allowed to reconstruct. These structures were then optimized using the aforementioned parameters until the forces on the atoms were reduced to 0.01 eV Å^{-1}.

Result and discussion

The crystallographic structures and phase purity of the as-prepared materials were investigated by p-XRD. The p-XRD spectra of the synthesized materials are given in Fig. 1a. The p-XRD spectra of CSs and NSCS samples showed the presence of two broad peaks appearing at 24.2° and 43.6° of 2θ corresponding to the (002) and (101) planes of graphitized carbon respectively. The p-XRD spectra of Co_3O_4, CS–Co_3O_4 and $NSCS$–
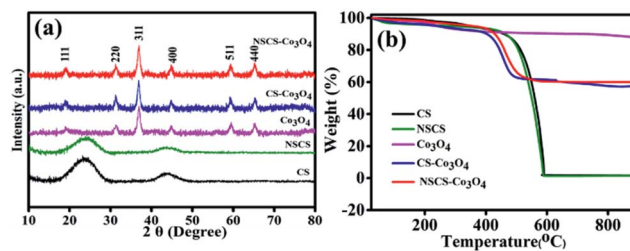

Fig. 1 (a) p-XRD pattern of CS, NSCS, Co_3O_4, CS–Co_3O_4 and $NSCS$–Co_3O_4. (b) TGA analysis of Co_3O_4, CS–Co_3O_4 and $NSCS$–Co_3O_4.

Co_3O_4 consist of peaks at 19.0°, 31.29°, 36.94°, 44.86°, 59.29° and 65.27° of 2θ corresponding to the (111), (220), (400), (511) and (440) planes respectively, indicating the Co_3O_4 spinel structure with a face-centred cubic lattice (JCPDS card no. 42-1467). Peaks of the CSs and NSCSs are not detected in the composite samples as the carbon spheres are completely covered by Co_3O_4 NPs. No residual/impurity peaks could be seen in the p-XRD spectra, indicating the good quality of the samples.

TGA was performed for all five samples in an air atmosphere at a rate of 10 °C min^{-1} up to 900 °C to quantify the weight percentage of individual components in the composites. In Fig. 1b, the weight loss below 150 °C can be attributed to the release of adsorbed moisture and gases from the surface of the samples.[25] CSs and NSCSs show complete weight loss after heating at 600 °C due to the formation of CO_2 in an oxygen atmosphere. In case of the CS–Co_3O_4 and $NSCS$–Co_3O_4 nano-composites, weight loss occurred from 400 °C to 500 °C and then showed a stable TGA profile, indicating the removal of carbon from the composites, and the residual peak corresponded to the weight percentage of Co_3O_4. Hence, Co_3O_4 and carbon contents in the composites are approximately 60% and 40% respectively.

X-ray photoelectron spectroscopic (XPS) analysis was carried out to find out the oxidation states of cobalt and elemental composition in the $NSCS$–Co_3O_4 composite. Fig. 2a shows the XPS survey spectra of the composite, which displays the presence of Co 2p, C 1s, N 1s and S 2p peaks. In Fig. 2b–e, core level peaks are further deconvoluted to understand the surface composition of the constituting elements. As shown in Fig. 2b, a combination of tetrahedral Co^{2+} and octahedral Co^{3+} contributes to the doublet 2p spectral profile of Co_3O_4 separated in high- and low-energy components due to spin–orbit coupling corresponding to $2p_{1/2}$ to $2p_{3/2}$ with a separation of 15.2 eV.[45,46] The deconvolution of the Co 2p peak at 779.3 eV and 780.6 eV is assigned to Co^{3+} $2p_{3/2}$ and Co^{2+} $2p_{3/2}$, respectively. The other spin–orbit components, Co^{3+} $2p_{1/2}$ and Co^{2+} $2p_{1/2}$, have been detected at 794.5 and 795.8 eV, respectively. The peaks at 782.1 eV and 797.3 eV may occur due to the chemical shift of the main spin–orbit components, resulting from the chemical interaction of Co cations with surface hydroxyl groups. In addition to these peaks, four small peaks are also observed corresponding to the shake-up satellite peaks of Co_3O_4 in the high-binding-energy side of $2p_{3/2}$ and $2p_{1/2}$ transitions,
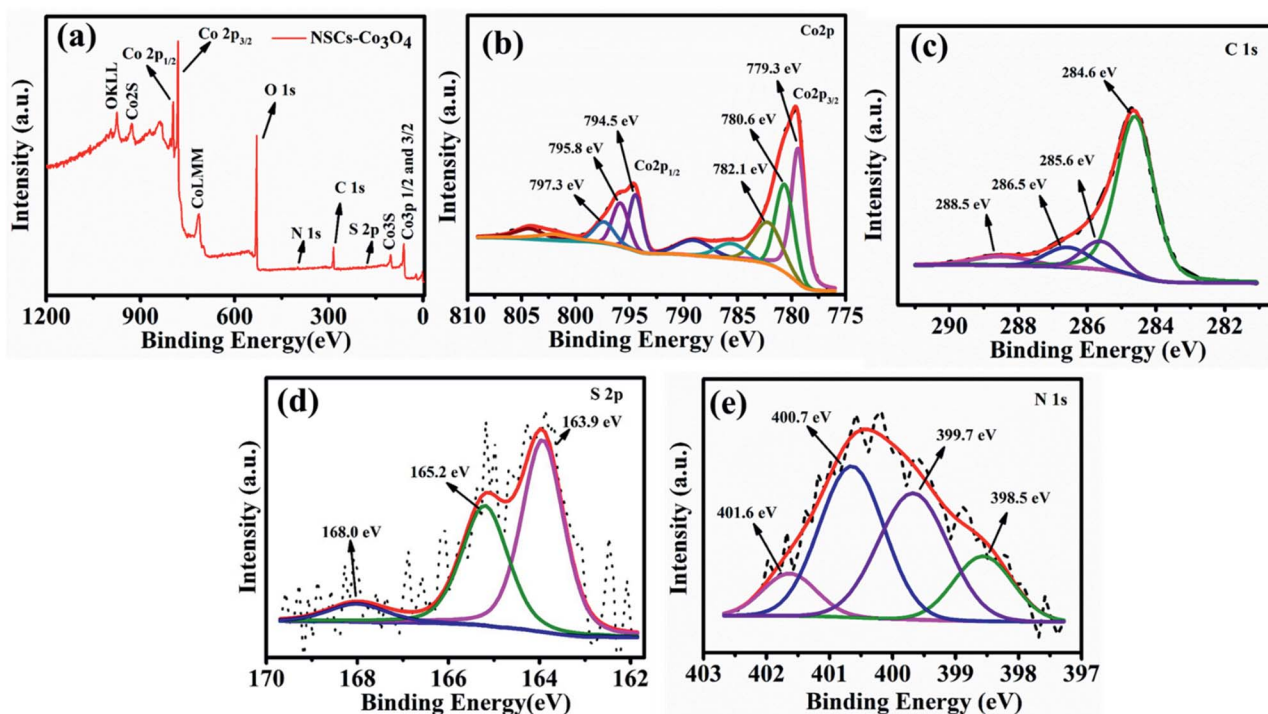
Fig. 2 (a) XPS survey scan of NSCS–Co$_3$O$_4$. Deconvoluted spectra of (b) Co 2p (c) C 1s (d) S 2p and (e) N 1s.

indicating the co-existence of Co(II) and Co(III) on the surface of the material. Fig. 2c shows four deconvolution peaks in the C 1s spectra at 284.6, 285.6, 286.5 and 288.5 eV, which correspond to the sp^2 hybridized carbon, sp^3 hybridized carbon, C–O/C–N and C=O bonds respectively.[47–49] The high-resolution S 2p spectra (Fig. 2d) show two peaks at 163.9 eV and 165.2 eV, which may correspond to the presence of C–S–C and C=S respectively and weak peaks at around 168 eV can be related to the oxidized sulfur.[50,51] The high-resolution N 1s spectrum (Fig. 2e) with four deconvoluted peaks at 398.5 eV, 399.7 eV, 400.7 eV and 401.6 eV could be attributed to the presence of pyridinic N, pyrrolic N, quaternary-graphitic N and oxidized species respectively.[52]

The surface and structural morphology of the as-prepared materials was observed by scanning electron microscopy (SEM), and the images are shown in Fig. 3. Fig. 3a represents the micron-sized particles of NSCSs. Fig. 3b shows Co$_3$O$_4$ NPs decorated on the surface of CSs. Here, Co$_3$O$_4$ NPs are distributed unevenly on the surface of CSs, leading to clustering, whereas in NSCS–Co$_3$O$_4$ (Fig. 3c), Co$_3$O$_4$ NPs are well distributed and homogeneously decorated on the NSCS surface forming an extended nanosheet-like structure, which uniformly covers the surface of NSCSs. It is also observable from the images that N and S doping is playing a vital role for the uniform nucleation and growth of Co$_3$O$_4$ nanoparticles by providing well-dispersed nucleation sites in NSCSs. Morphological control on the uniform growth of Co$_3$O$_4$ NPs through N and S doping can be highlighted using atomic distribution of different elements over the surface of NSCS–Co$_3$O$_4$. SEM elemental maps are shown in Fig. S1a–f,† which indicate the presence of all five elements (Co, C, N, S and O) that are homogeneously distributed throughout the sample.

Transmission electron microscopic (TEM) characterization was performed on all samples to provide an insight into the inner architecture and crystallographic structure of the as-prepared materials. Fig. 3d represents the TEM image of well-dispersed N- and S-doped carbon spheres with a diameter ranging between 2 and 5 micrometres. Fig. 3e shows the Co$_3$O$_4$ nanoparticles with 10–20 nm size. The higher magnification image in Fig. 3f clearly verifies the cubic structure of Co$_3$O$_4$ NPs with interplanar spacings of 0.28 nm and 0.24 nm, corresponding to the (220) and (311) planes of the face-centred cubic phase of Co$_3$O$_4$, respectively.[53] Fig. 3g shows that N and S co-doped carbon spheres are closely and densely surrounded by Co$_3$O$_4$ NPs, which are extended into sheet-like structures due to uniform coverage over the NSCS surface. The high-magnification image (Fig. 3h) of NSCS–Co$_3$O$_4$ also reveals the surface boundary of NSCSs and Co$_3$O$_4$ NPs aggregated like sheets, which indicates the homogeneous distribution of Co$_3$O$_4$ NPs on the surface of NSCSs. Fig. 3i illustrates the typical selected-area electron diffraction (SAED) pattern of the NSCS–Co$_3$O$_4$ nanocomposites. The diffraction rings correspond to (220), (311), (400), (511), and (440) planes of polycrystalline Co$_3$O$_4$.[54]

Lithium storage properties of Co$_3$O$_4$, CS–Co$_3$O$_4$ and NSCS–Co$_3$O$_4$ composites were examined in a coin cell configuration versus Li/Li$^+$ under identical conditions, and the results are shown in Fig. 4a–e. The cyclic voltammetry (CV) measurements for Co$_3$O$_4$, CS–Co$_3$O$_4$ and NSCS–Co$_3$O$_4$ composite electrodes were performed at a scan rate of 0.25 mV s^{-1} in the potential window of 0.01 V to 3.0 V. A distinct and irreversible reduction peak appeared at 0.77 V in the first cathodic scan of the Co$_3$O$_4$
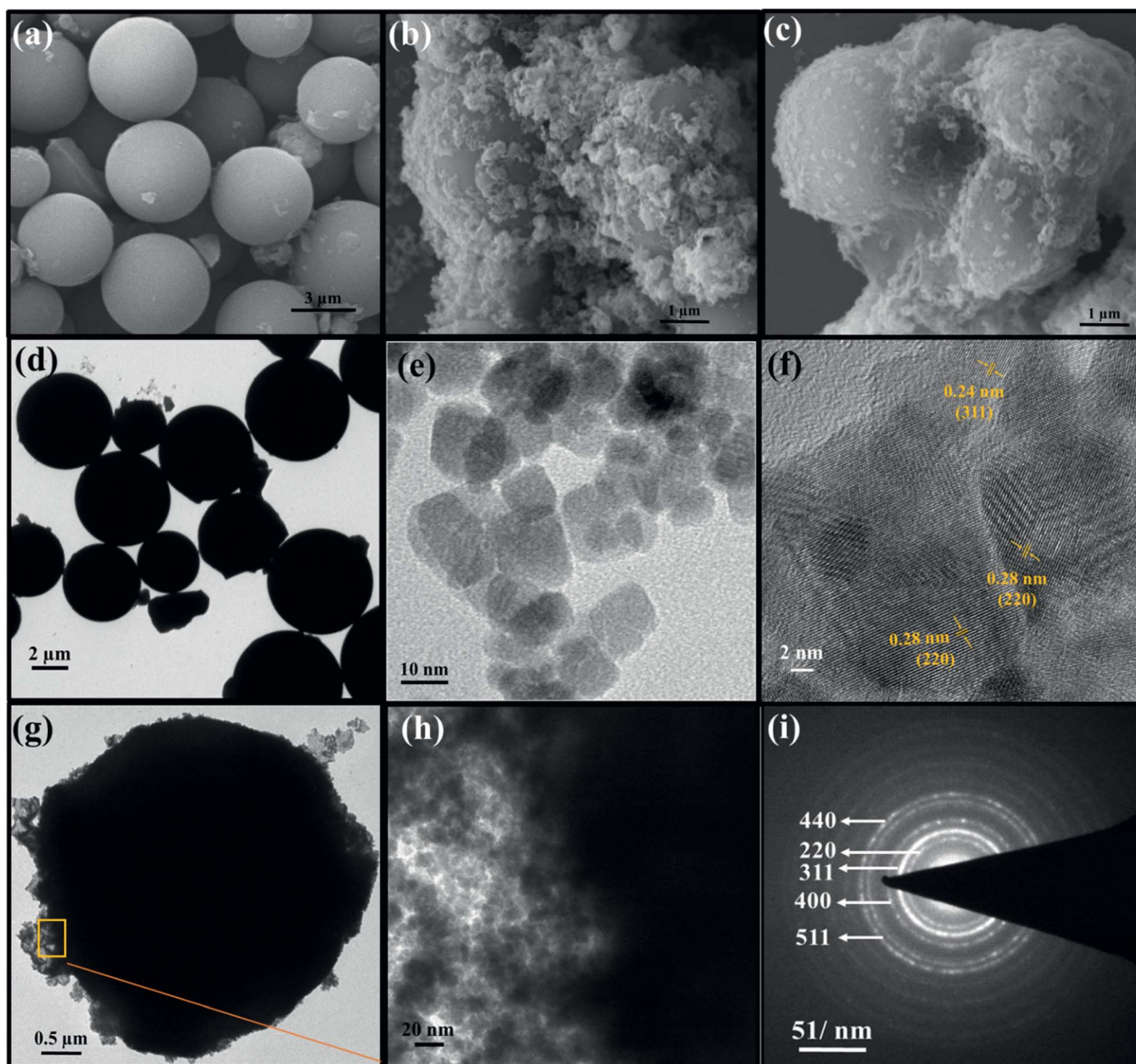
Fig. 3 ESEM images of (a) NSCS, (b) CS−Co_3O_4 and (c) NSCS−Co_3O_4, TEM images of (d) NSCS, (e) low- and (f) high-resolution images of Co_3O_4 nanoparticles, (g) low-resolution image of NSCS−Co_3O_4, (h) high-resolution image of NSCS−Co_3O_4, and (i) SAED pattern of NS−Co_3O_4.

CV curve (Fig. 4a) due to the reduction of Co_3O_4 to metallic Co and the formation of amorphous Li_2O by a conversion reaction. Simultaneous decomposition of electrolytes takes place to form a solid electrolyte interphase (SEI) layer on the surface of the electrode.[26,27] From the second cycle onwards, cathodic peak split into two distinguishable peaks appearing nearly at 1.01 V and 1.23 V with a lesser intensity, which is due to a multistep reaction during lithiation and the presence of some irreversible transformation that gives structural modification in the first cycle.[26,27,34] Moreover, two broad peaks are observed during an anodic scan at potentials of 1.35 V and 2.1 V, which could be attributed to the oxidation of metallic Co. The electrochemical reaction mechanism of Co_3O_4 involves the formation and decomposition of Li_2O, accompanied by the reduction of Co^{3+} to Co^{2+} and Co^{2+} to Co and the oxidation of Co to Co^{2+} and Co^{2+}

to Co^{3+} through an intermediate of CoO. This multiple electron process can be represented by eqn (2) and (3).[55]

$$Co_3O_4 + 2Li^+ + 2e^- \leftrightarrow Li_2O + 3CoO \quad (2)$$

$$3CoO + 6Li^+ + 6e^- \leftrightarrow 3Li_2O + 3Co \quad (3)$$
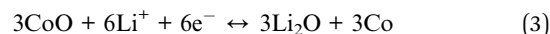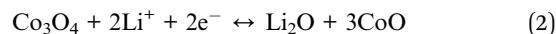
In case of the CS−Co_3O_4 electrode, as shown in Fig. 4b, during the first cathodic scan, a reduction peak was observed at 0.71 V and subsequent cathodic peaks (2nd cycle onwards) were observed at 0.87 V and 1.29 V *vs.* Li/Li^+, whereas the anodic peaks were obtained at approximately 1.37 V and 2.14 V. Fig. 4c represents the CV curve of the NSCS−Co_3O_4 composite, where the first cathodic peak appeared at 0.85 V and subsequent
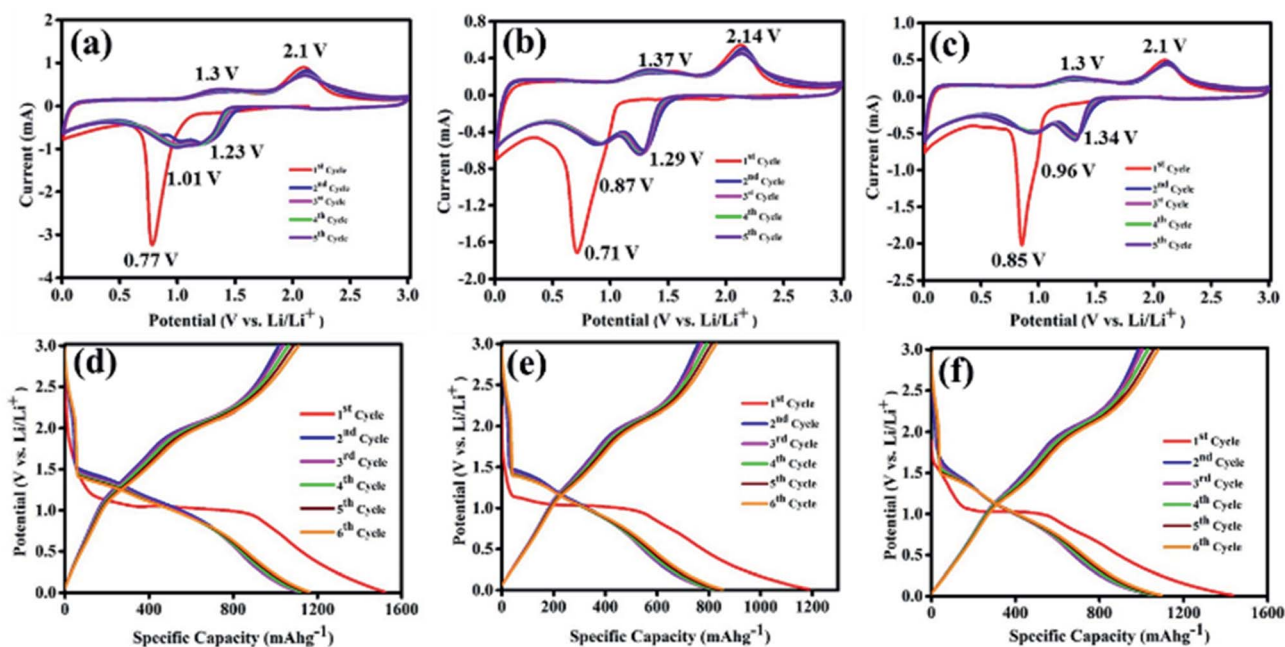
Fig. 4 Cyclic voltammetry curves of (a) Co_3O_4 nanoparticles, (c) CS–Co_3O_4 and (e) NSCS–Co_3O_4 composite electrodes over 6 cycles at a scan rate of 0.25 mV s^{-1} and potential range of 0.01–3.0 V vs. (Li/Li$^+$). Galvanostatic charge–discharge profiles of (b) Co_3O_4 nanoparticles, (d) CS–Co_3O_4 and (f) NSCS–Co_3O_4 composite electrodes at a current density of 100 mA g^{-1}.

cathodic peaks appeared at 0.96 and 1.34 V, whereas anodic peaks were observed at 1.3 V and 2.1 V. In the NSCS–Co_3O_4 composite, the subsequent cycles represent the proper overlapping of anodic and cathodic peaks, an indication of the good electrochemical reversibility of the electrode material.

The galvanostatic charge–discharge (GCD) curves are shown in Fig. 4d, e and f for Co_3O_4, CS–Co_3O_4 and NSCS–Co_3O_4 respectively within a voltage window of 0.01–3.00 V (vs. Li/Li$^+$). The GCD curves were recorded at a current density of 100 mA g^{-1}, and the obtained results are in well accordance with the CV results. In the charge–discharge profiles of Co_3O_4, CS–Co_3O_4 and NSCS–Co_3O_4, an extended voltage plateau is observed at around 1.1 V, resulting from the lithiation of Co_3O_4 and the formation of Co and Li_2O. In the charge curves, the slope region from 1.2 to 2.5 V corresponds to the reversible oxidation of Co_3O_4. Discharge capacity values calculated from the second cycle are around 1106 mA h g^{-1}, 836 mA h g^{-1} and 1075 mA h g^{-1} for Co_3O_4, CS–Co_3O_4 and NSCS–Co_3O_4 respectively. A lower specific capacity value of CS–Co_3O_4 compared to bare Co_3O_4 is probably due to the addition of CSs, but in case of NSCS–Co_3O_4, reversible capacity increases due to N and S co-doping in CSs, which may provide a large number of edge defects with enhanced electronic conductivity and improved lithium-ion accessibility.[34] Another reason could be the homogeneous distribution of Co_3O_4 nanoparticles on the surface of NSCSs, which may allow better charge transfer.

Impedance measurements of Co_3O_4, CS–Co_3O_4 and NSCS–Co_3O_4 electrodes were carried out in the frequency range of 100 kHz to 0.05 Hz at room temperature. As shown in Fig. 5a, Nyquist plots of all three electrodes consist of a depressed semicircle at the high-frequency region and an inclined line at
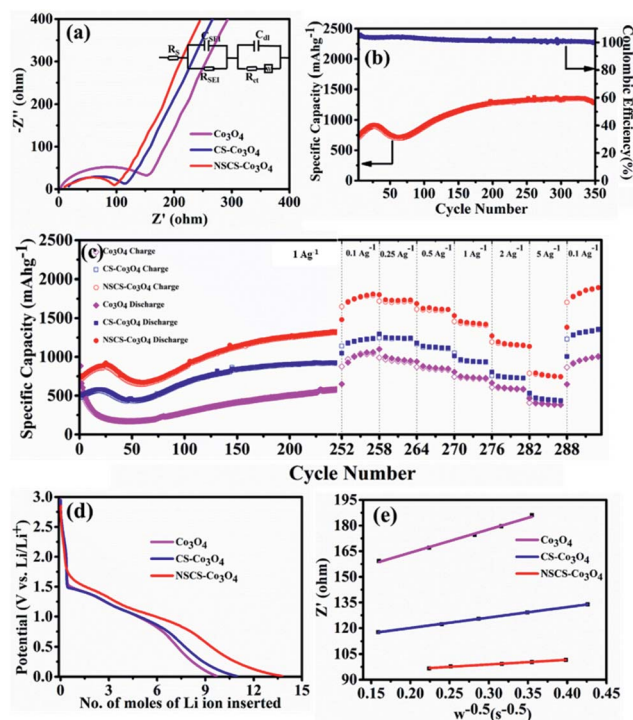
Fig. 5 (a) Impedance spectra of Co_3O_4, CS–Co_3O_4 and NSCS–Co_3O_4. (b) Cyclic stability of NSCS–Co_3O_4 at 1 A g^{-1}. (c) Rate performance of Co_3O_4, CS–Co_3O_4 and NSCS–Co_3O_4. (d) Relationship between voltage and x mole of Li insertion in the second discharge curve of Co_3O_4, CS–Co_3O_4 and NSCS–Co_3O_4. (e) Relationship between real resistance and frequency of Co_3O_4, CS–Co_3O_4 and NSCS–Co_3O_4.

the low-frequency region. The high-frequency semicircle is attributed to the SEI film formation, contact resistance, and charge transfer resistance on the electrode/electrolyte interface, whereas the inclined line in the low-frequency region corresponds to the lithium-diffusion process within electrodes.[56] The charge transfer resistance is calculated by the fitting circuit model. It is observed to be lower for NSCS–Co_3O_4 (65.72 Ω) as compared to bare Co_3O_4 (152.5 Ω) and CS–Co_3O_4 (106.1 Ω), implying more conducting nature and faster Li^+ diffusion rate of NSCS–Co_3O_4 nanocomposites. Reduced charge transfer resistance of NSCS–Co_3O_4 electrodes is possibly due to the carbon matrix, which reduces the mechanical strain and avoids volume expansion during the charge–discharge process. Additionally, N and S co-doping enhances the electronic conductivity, providing continuous and rapid electron transport, which may accelerate the Li ion storage capacity of the electrode material. Fig. 5b shows the cyclability of NSCS–Co_3O_4 composites at a current density of 1 A g^{-1} for 350 cycles. It can be observed that the as-prepared NSCS–Co_3O_4 electrode exhibits long cycle life over 350 cycles with higher specific capacity value and nearly 100% of coulombic efficiency. Over the cycling, more reactive sites of NSCS–Co_3O_4 are activated and contributing in lithium-ion storage, which is reflected in the gradually increasing specific capacity up to 919 mA h g^{-1} for initial 25 cycles. Additionally, heteroatom-doped carbon spheres provide more reactive sites, leading to the increased lithium-ion storage capacity while cycling.[56–58] Afterwards, for 70 cycles, the capacity value decreases to 720 mA h g^{-1}, which may be due to the deterioration of the electrode material on the continuous charge–discharge process, resulting in increased charge transfer resistance which is an inherent characteristic of the TMO electrodes.[35,59] A further increase in capacity value was observed up to 250 cycles (1331 mA h g^{-1}), which remained stable over 350 cycles with 96.5% capacity retention as well as >99% coulombic efficiency. This increasing trend in the discharge capacity is probably due to the enhanced kinetics of Li ion diffusion by the gradual activation process and the formation of the polymeric gel-like film with better electrolyte infiltration during cycling.[60] Moreover, heteroatom-doped carbon spheres reduce the volume expansion during cycling and provide structural stability to Co_3O_4 NPs. NSCSs increase the electronic and ionic conductivities of the composite electrode, leading to fast Li^+ insertion kinetics in Co_3O_4.[34] A similar trend was observed in another composite anode CS–Co_3O_4 though with lesser specific capacity than NSCS–Co_3O_4. Therefore, the rate performance of these materials was analysed after 250 cycles. Fig. 5c illustrates the comparative rate performance of the Co_3O_4, CS–Co_3O_4 and NSCS–Co_3O_4 electrodes after 251 continuous charge–discharge cycles at 1 A g^{-1} and varying current densities between 0.1 A g^{-1} and 5 A g^{-1}. Among all, NSCS–Co_3O_4 electrodes exhibit excellent rate performance with reversible discharge capacities of 1807, 1730, 1616, 1419, and 1151 mA h g^{-1} at 0.1, 0.25, 0.5, 1 and 2 A g^{-1}, respectively. Even at a high current density of 5 A g^{-1}, the NSCS–Co_3O_4 electrode delivers a high specific capacity of 745 mA h g^{-1}. However, bare Co_3O_4 electrodes exhibit a specific capacity of 1060 mA h g^{-1} at 0.1 A g^{-1} and 384 mA h g^{-1} at 5 A g^{-1}, while CS–Co_3O_4 composite electrodes deliver a specific capacity of 1237 mA h g^{-1} at 0.1 A g^{-1} and 437 mA h g^{-1} at 5 A g^{-1}. When current density reverted to 0.1 A g^{-1}, NSCS–Co_3O_4 gives

1889 mA h g^{-1} of specific capacity after 292 cycles, whereas Co_3O_4 and CS–Co_3O_4 deliver 1007 and 1356 mA h g^{-1} of specific capacity. The enhanced rate performance of the NSCS–Co_3O_4 nanocomposites could be ascribed to the improved electron transfer due to nanostructured cobalt oxides and the increased electronic conductivity provided by the conducting carbon network, fast kinetics, and reduced volume expansion at a higher current density of the NSCS in the nanocomposites.[34] Hence, from Fig. 5c, it can be clearly observed that in comparison to Co_3O_4 and CS–Co_3O_4, NSCS–Co_3O_4 shows excellent rate performance at high current density, which is the result of doped nitrogen and sulphur in carbon.

Furthermore, the Li ion diffusion coefficient (D_{Li^+}) of the cell was calculated using the following eqn (4):[61]

$$D_{Li^+} = \frac{1}{2}\{V_m/AF\sigma_w \times \partial E/\partial x\}^2 \qquad (4)$$

where V_m is the molar volume, A is the area of the electrode surface (1.13 cm^2), F is the Faraday constant (96 500 coulomb mol^{-1}), σ_w is the Warburg coefficient and $\partial E/\partial x$ is the slope of potential vs. Li concentration plot as shown in Fig. 5d. σ is obtained from the extrapolation of the straight line in the lower frequency region from the semicircle to real axis.[62]

$$Z_{re} = R_e + R_{ct} + \sigma\omega^{-0.5} \qquad (5)$$

where σ is the slope for the plot of Z_{re} vs. the reciprocal root square of the lower angular frequencies ($\omega^{-0.5}$), as shown in Fig. 5e. The obtained values for σ are 141.422, 39.8 and 27.422 for Co_3O_4, CS–Co_3O_4 and NSCS–Co_3O_4, respectively. As shown in Table 1, the achieved Li ion diffusion coefficients of Co_3O_4, CS–Co_3O_4 and NSCS–Co_3O_4 are 1.23×10^{-13} cm^2 s^{-1}, 0.56×10^{-12} and 1.73×10^{-12} cm^2 s^{-1} respectively. Among them, the NSCS–Co_3O_4 composite is having a higher Li ion diffusion coefficient than other electrode materials, which agree with the other electrochemical performances. Heteroatom-doped carbon spheres could increase the kinetics of Li ions on the electrode surface by improving the conductivity of the electrode material, which helps to improve the electrochemical performance of the battery.

To understand the effect of charge–discharge cycling on the cell after 350 cycles, we have performed the impedance measurement (Fig. S4a†) and TEM study (Fig. S4b and c†), and the corresponding figures and discussion are given in ESI.†

Computational study

The computed crystal structure of Co_3O_4 with the Hubbard U correction was verified against the experimentally reported

Table 1 Values of σ_w, X, and D_{Li} for Co_3O_4, CS–Co_3O_4 and NSCS–Co_3O_4 as determined from EIS data

Electrode	σ_w (Ω s$^{-1/2}$)	X (mol cm^{-3})	D_{Li} (cm^2 s^{-1})
Co_3O_4	135.96	0.1852	0.123×10^{-12}
CS–Co_3O_4	61.24	0.1768	0.56×10^{-12}
NSCS–Co_3O_4	27.42	0.1394	1.73×10^{-12}

structure. The deviation between the computed and experimental lattice parameters is found to be less than 0.1%, confirming that the parameters and methodology utilized are appropriate. As stated, the Li-atoms were added to the structure, in steps of eight atoms. Hence, the initial structure has 8 Li-atoms, while the fully lithiated Co_3O_4 structure has 64 Li-atoms. The lithiation strategy was modeled in accordance with eqn (2) and (3) representing the chemical reaction. Some representative models are shown in Fig. 6a–d for Co_3O_4, Fig. 6e–h for CS–Co_3O_4 and Fig. 6i–l for NSCS–Co_3O_4.

A trend of increase in the volume of the crystal structure (Co_3O_4) is observed with the increase in number of Li-atoms. The volume of the bulk system is 573.57 Å^3, while the volume of the fully lithiated structure is 1421.70 Å^3. An increase of approximately 248% is observed. CS–Co_3O_4 and NSCS–Co_3O_4 structures were also lithiated to investigate the effect of the substrate as well as doping on the volume expansion and overall functioning of the electrode. Volume expansion upon lithiation, in CS–Co_3O_4 and NSCS–Co_3O_4 systems, is significantly lower than that of bulk Co_3O_4. The initial volume of CS–Co_3O_4 and NSCS–Co_3O_4 systems was 790.832 Å^3 and 808.515 Å^3 respectively, which increased to 1628.31 Å^3 and 1618.36 Å^3, respectively upon lithiation. The percentage volume expansion was found to be 206% and 200% for CS–Co_3O_4 and NSCS–Co_3O_4 respectively. A considerable downshift in volume expansion upon lithiation underlines the role of support in restraining the volume as compared to unsupported Co_3O_4. A downshift in the volume expansion and the corresponding ΔE_{mix} value reflect the enhanced stability of the system. In Fig. 7a, the ΔE_{mix} value (on the left y-axis) and change in volume (on the right y-axis) have been plotted against the number of Li atoms added to the system. The change in volume is considerably less in the composite systems compared to Co_3O_4. The support provides additional strength to the lattice of Co_3O_4 by providing an anchoring point. The presence of the support for Co_3O_4 results in bonding between C and Co as well as between C and O, thus restricting the expansion of at least Co and

O atoms in contact with the support upon lithiation. This does reflect the lesser volume expansion for supported systems. The support also affects the functioning of Co_3O_4 in terms of slowing down the reaction from Co_3O_4 to CoO-like phase. This could be understood from the analysis of Co–O bonds as a function of lithiation in these three systems. In Fig. 7b, we have shown the shortest Co–O bonds as a function of increasing Li contents in the system. In the case of Co_3O_4, a sudden shift in the number of short Co–O bonds is observed, while the number of Li atoms within the system changes from 8 to 16. There are about 103 short Co–O bonds in the Co_3O_4 + 8 Li system. This number drastically reduces to 55 in case of the Co_3O_4 + 16 Li system. Furthermore, the long-range order in the system is lost as evident from the continuous distribution of the bond lengths. This sudden shift marks the transition from Co_3O_4 to CoO-like phase. It is interesting to note the effect of the support on the Co–O bond lengths in CS–Co_3O_4. The bare (or unlithiated) CS–Co_3O_4 has less number of Co–O short bonds compared to unsupported Co_3O_4 because Co, as well as O, gets bonded with the support. However, upon lithiation, the transition is slowed down, as reflected from the Co–O bond lengths shown in Fig. 7c. For 16 Li atoms in CS–Co_3O_4, there are 64 short Co–O bonds, which were about 55 in case of unsupported Co_3O_4, indicating 10–15% reduction in Co–O short bonds. This marks the negative effect of support which although helps in controlling the volume expansion but only at the cost of Li holding capacity and therefore showing reduced performance. However, when we compare it with NSCS–Co_3O_4, the number of Co–O short bonds upon addition of 16 Li atoms are about 57, indicating that the behaviour of NSCS–Co_3O_4 is similar to that of unsupported Co_3O_4 (Fig. 7d). Thus, Co_3O_4 placed over N and S doped carbon reduces the volume expansion and does not compromise on the Li holding capacity as much as in the case of CS–Co_3O_4.

The specific capacity of the Co_3O_4 system can be related to its ability to undergo reactions in order to form CoO and Li_2O and finally CoO getting converted into metallic Co (as given by eqn (1) and (2)). As lithiation progresses, Co_3O_4 gets converted into CoO and finally into metallic Co, as discussed above. In terms of effective charge on Co, it changes from Co^{3+} to Co^{2+} in CoO and then to metallic Co^0 upon complete lithiation. This transition also reflects the Bader charges as well as Co–O bond lengths as a function of lithiation.

Our detailed DFT calculations demonstrate that the presence of the support below the Co_3O_4 nanoparticle does play an important role, in controlling both the volume expansion and the specific capacity. The carbon support holds the Co and O atoms that not only restrain volume expansion but also decrease the interaction of Li atoms with cobalt and oxygen, which would have otherwise lead to the conversion of Co_3O_4 into CoO and further into metallic Co. However, the presence of dopants have helped in controlling the formation of C–Co bonds, such that Li atoms can interact in a better way with the Co and O atoms to form CoO and metallic Co without resisting its capability to reduce volume expansion.

In summary, the excellent electrochemical performance of NSCS–Co_3O_4 could be attributed to the synergetic effect of Co_3O_4 and N and S co-doped carbon spheres. Nanoparticles of Co_3O_4 effectively reduce the path length for lithium-ion
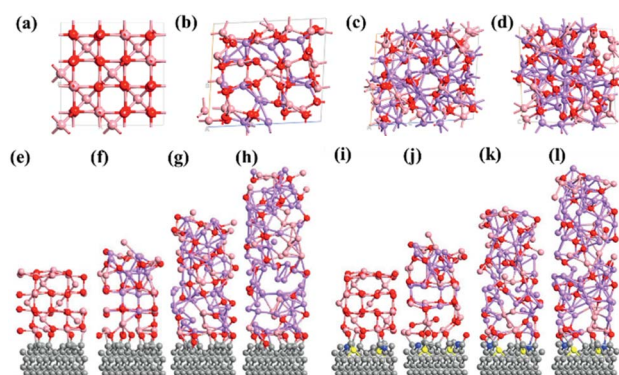

Fig. 6 (a–d) Bulk Co_3O_4 with 0, 16, 40, and 64 Li atoms respectively. The pink-coloured balls represent Co atoms, red-coloured balls represent oxygen and violet-coloured balls represent Li atoms. Comparison between (a) and (d) shows a complete reordering of the Co_3O_4 crystal lattice. (e–h) CS–Co_3O_4, with 0, 16, 40, and 64, Li atoms alloyed, respectively. Similarly, (i–l) NSCS–Co_3O_4, with 0, 16, 40, and 64 Li atoms, respectively.
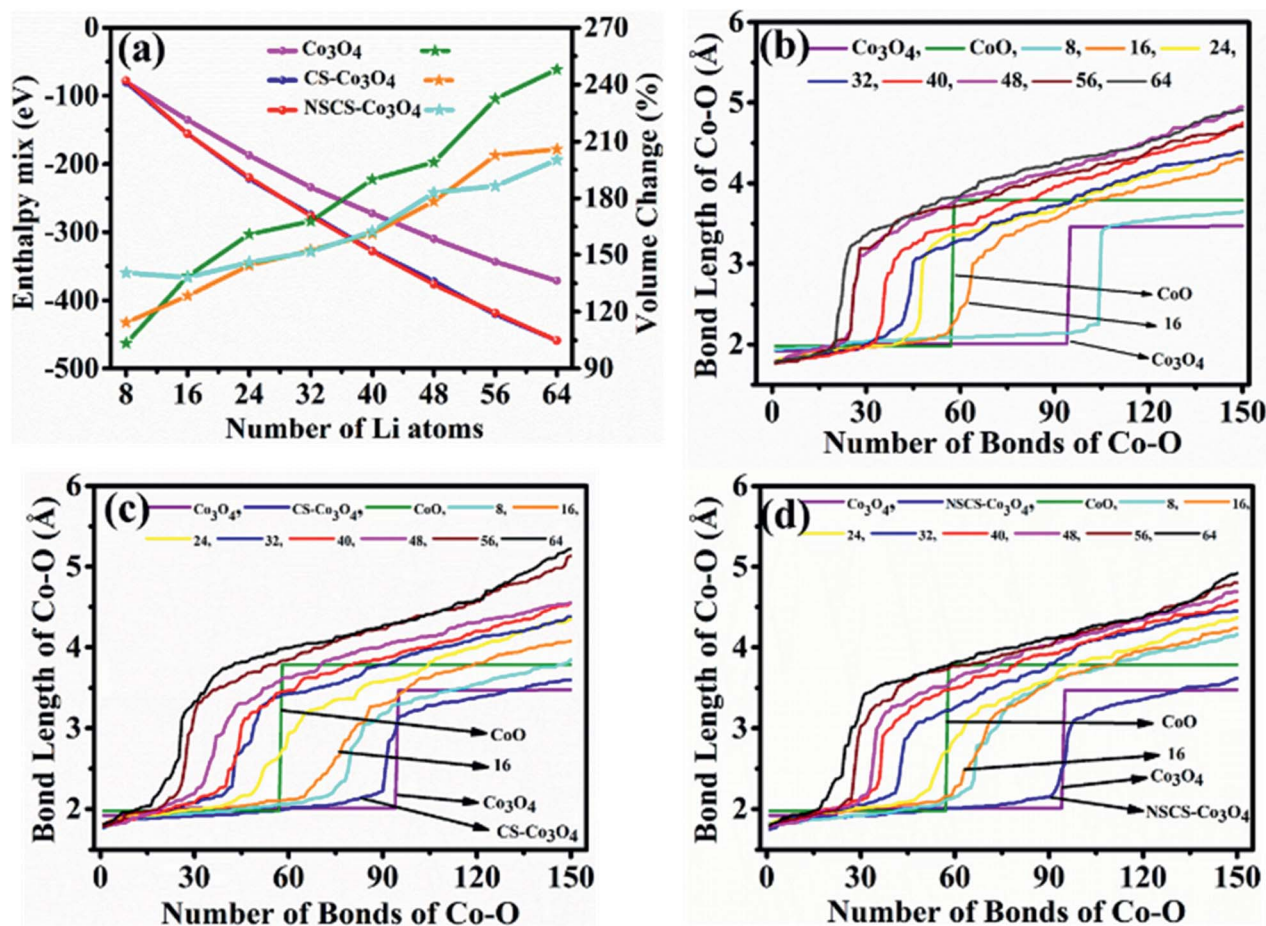
Fig. 7 (a) Enthalpy of alloy formation (ΔE_{mix}) and change in volume of Co_3O_4, $CS–Co_3O_4$ and $NSCS–Co_3O_4$ with respect to the number of Li atoms. The Co–O distance in (b) Co_3O_4, (c) $CS–Co_3O_4$, and (d) $NSCS–Co_3O_4$ as a function of lithiation. The Co–O bonds in crystalline Co_3O_4 and CoO are plotted for reference. In case of bulk-Co_3O_4 and $NSCS–Co_3O_4$, the CoO phase is more dominant from 16 Li onwards, whereas, in case of $CS–Co_3O_4$, the formation of the CoO-like phase is delayed and appears to dominate from 24 Li onwards.

migration during the charge/discharge process. Heteroatom doping offers suitable pathways for electron transfer and provides a good conductive matrix for Co_3O_4 nanoparticles. NSCSs also act as a buffer substrate to accommodate the volume changes of Co_3O_4 in the process of lithium-ion insertion/extraction. Nitrogen and sulphur doping introduce defects, thus leading to the formation of disordered carbon structure, which tends to be electron accepting and provides anchor sites for the Co_3O_4 nanoparticles.

Conclusions

An $NSCS–Co_3O_4$ nanocomposite has been synthesized as an anode material with a significant potential for application in lithium-ion batteries as a high-energy material. Doped N and S atoms enhance the electronic conductivity and also provide binding sites for the facile deposition of a large number of Co_3O_4 nanoparticles. It also provides the channels for charge and ionic transport, which effectively alleviates the aggregation of Co_3O_4 in the Li^+ insertion/extraction. As a result, $NSCS–Co_3O_4$ shows excellent rate performance and long cycle life. Among all

the three electrodes, $NSCS–Co_3O_4$ exhibits less charge transfer resistance with a higher Li ion diffusion coefficient value of 1.73×10^{-12} cm^2 s^{-1}.

Conflicts of interest

The authors declare no competing financial interest.

Acknowledgements

References

1 R. Marom, S. F. Amalraj, N. Leifer, D. Jacob and D. Aurbach, *J. Mater. Chem.*, 2011, **21**, 9938–9954.
2 M. Armand and J.-M. Tarascon, *Nature*, 2008, **451**, 652.

3 S. Goriparti, E. Miele, F. De Angelis, E. Di Fabrizio, R. Proietti Zaccaria and C. Capiglia, *J. Power Sources*, 2014, **257**, 421–443.

4 D. P. Dubal, O. Ayyad, V. Ruiz and P. Gomez-Romero, *Chem. Soc. Rev.*, 2015, **44**, 1777–1790.

5 J. Jiang, Y. Li, J. Liu and X. Huang, *Nanoscale*, 2011, **3**, 45–58.

6 A. S. Aricò, P. Bruce, B. Scrosati, J.-M. Tarascon and W. van Schalkwijk, *Nat. Mater.*, 2005, **4**, 366.

7 L. Zhang, H. Bin Wu and X. W. Lou, *Adv. Energy Mater.*, 2013, **4**, 1300958.

8 J. Ming, J.-B. Park and Y.-K. Sun, *ACS Appl. Mater. Interfaces*, 2013, **5**, 2133–2136.

9 Y. Wang, B. Wang, F. Xiao, Z. Huang, Y. Wang, C. Richardson, Z. Chen, L. Jiao and H. Yuan, *J. Power Sources*, 2015, **298**, 203–208.

10 M. R. Palacín, *Chem. Soc. Rev.*, 2009, **38**, 2565–2575.

11 D. Gu, W. Li, F. Wang, H. Bongard, B. Spliethoff, W. Schmidt, C. Weidenthaler, Y. Xia, D. Zhao and F. Schüth, *Angew. Chem.*, 2015, **127**, 7166–7170.

12 Y. Huang, C. Chen, C. An, C. Xu, Y. Xu, Y. Wang, L. Jiao and H. Yuan, *Electrochim. Acta*, 2014, **145**, 34–39.

13 L. Zhan, S. Wang, L.-X. Ding, Z. Li and H. Wang, *Electrochim. Acta*, 2014, **135**, 35–41.

14 J. Guo, L. Chen, X. Zhang and H. Chen, *J. Solid State Chem.*, 2014, **213**, 193–197.

15 L. Tian, H. Zou, J. Fu, X. Yang, Y. Wang, H. Guo, X. Fu, C. Liang, M. Wu, P. K. Shen and Q. Gao, *Adv. Funct. Mater.*, 2010, **20**, 617–623.

16 K. Qiu, J. Lu, J. Cheng, H. Yan, X. Hou, D. Zhang, M. Lu, X. Liu and Y. Luo, *Electrochim. Acta*, 2015, **157**, 62–68.

17 D. Liu, X. Wang, X. Wang, W. Tian, Y. Bando and D. Golberg, *Sci. Rep.*, 2013, **3**, 2543.

18 X. Liu, Q. Long, C. Jiang, B. Zhan, C. Li, S. Liu, Q. Zhao, W. Huang and X. Dong, *Nanoscale*, 2013, **5**, 6525–6529.

19 Y. Zhang, Y. Wu, Y. Chu, L. Li, Q. Yu, Y. Zhu, G. Liu, Q. Hou, R. Zeng and L. Zhao, *Electrochim. Acta*, 2016, **188**, 909–916.

20 G. Huang, S. Xu, S. Lu, L. Li and H. Sun, *ACS Appl. Mater. Interfaces*, 2014, **6**, 7236–7243.

21 S. Abouali, M. Akbari Garakani, B. Zhang, H. Luo, Z.-L. Xu, J.-Q. Huang, J. Huang and J.-K. Kim, *J. Mater. Chem. A*, 2014, **2**, 16939–16944.

22 J. Xu, J. Wu, L. Luo, X. Chen, H. Qin, V. Dravid, S. Mi and C. Jia, *J. Power Sources*, 2015, **274**, 816–822.

23 Y. Liu, Z. Cheng, H. Sun, H. Arandiyan, J. Li and M. Ahmad, *J. Power Sources*, 2015, **273**, 878–884.

24 X. Zhou, J. Shi, Y. Liu, Q. Su, J. Zhang and G. Du, *Electrochim. Acta*, 2014, **143**, 175–179.

25 Y. Lou, J. Liang, Y. Peng and J. Chen, *Phys. Chem. Chem. Phys.*, 2015, **17**, 8885–8893.

26 G. Huang, F. Zhang, X. Du, Y. Qin, D. Yin and L. Wang, *ACS Nano*, 2015, **9**, 1592–1599.

27 L. Shen and C. Wang, *Electrochim. Acta*, 2014, **133**, 16–22.

28 X. Liu, S. W. Or, C. Jin, Y. Lv, W. Li, C. Feng, F. Xiao and Y. Sun, *Electrochim. Acta*, 2013, **100**, 140–146.

29 K. Sun, Y. Hu, X. Zhang, K. San Hui, K. Zhang, G. Xu, J. Ma and W. He, *Electrochim. Acta*, 2020, **335**, 135680.

30 X. Zhang, Z. Bi, G. Xu, C. Li, W. He and J. Zhu, *J. Power Sources*, 2019, **438**, 226980.

31 X. Yi, W. He, X. Zhang, G. Yang and Y. Wang, *J. Alloys Compd.*, 2018, **735**, 1306–1313.

32 L. Wang, Y. Zheng, X. Wang, S. Chen, F. Xu, L. Zuo, J. Wu, L. Sun, Z. Li, H. Hou and Y. Song, *ACS Appl. Mater. Interfaces*, 2014, **6**, 7117–7125.

33 Y. Sun, F. Huang, S. Li, Y. Shen and A. Xie, *Nano Res.*, 2017, **10**, 3457–3467.

34 L. Guo, Y. Ding, C. Qin, W. Li, J. Du, Z. Fu, W. Song and F. Wang, *Electrochim. Acta*, 2016, **187**, 234–242.

35 D. Li, D. Shi, Z. Chen, H. Liu, D. Jia and Z. Guo, *RSC Adv.*, 2013, **3**, 5003–5008.

36 Y. Fang, R. Liu, L. Zeng, J. Liu, L. Xu, X. He, B. Huang, Q. Chen, M. Wei and Q. Qian, *Electrochim. Acta*, 2019, **318**, 737–745.

37 L. Zeng, B. Kang, F. Luo, Y. Fang, C. Zheng, J. Liu, R. Liu, X. Li, Q. Chen, M. Wei and Q. Qian, *Chem.–Eur. J.*, 2019, **25**, 13411–13421.

38 G. Kresse and D. Joubert, *Phys. Rev. B: Condens. Matter Mater. Phys.*, 1999, **59**, 1758–1775.

39 J. Paier, M. Marsman, K. Hummer, G. Kresse, I. C. Gerber and J. G. Ángyán, *J. Chem. Phys.*, 2006, **124**, 154709.

40 G. Kresse and J. Furthmüller, *Phys. Rev. B: Condens. Matter Mater. Phys.*, 1996, **54**, 11169–11186.

41 G. Kresse and J. Furthmüller, *Comput. Mater. Sci.*, 1996, **6**, 15–50.

42 G. Kresse and J. Hafner, *Phys. Rev. B: Condens. Matter Mater. Phys.*, 1993, **47**, 558–561.

43 A. Jain, S. P. Ong, G. Hautier, W. Chen, W. D. Richards, S. Dacek, S. Cholia, D. Gunter, D. Skinner, G. Ceder and K. A. Persson, *APL Mater.*, 2013, **1**, 11002.

44 H. Kim, C.-Y. Chou, J. G. Ekerdt and G. S. Hwang, *J. Phys. Chem. C*, 2011, **115**, 2514–2521.

45 X. Tian, X. Sun, Z. Jiang, Z.-J. Jiang, X. Hao, D. Shao and T. Maiyalagan, *ACS Appl. Energy Mater.*, 2018, **1**, 143–153.

46 C. K. Ranaweera, C. Zhang, S. Bhoyate, P. K. Kahol, M. Ghimire, S. R. Mishra, F. Perez, B. K. Gupta and R. K. Gupta, *Mater. Chem. Front.*, 2017, **1**, 1580–1584.

47 Z. Yang, K. Qian, J. Lv, W. Yan, J. Liu, J. Ai, Y. Zhang, T. Guo, X. Zhou, S. Xu and Z. Guo, *Sci. Rep.*, 2016, **6**, 27957.

48 L. Zhang, Z. Su, F. Jiang, L. Yang, J. Qian, Y. Zhou, W. Li and M. Hong, *Nanoscale*, 2014, **6**, 6590–6602.

49 D. Bhattacharjya, H.-Y. Park, M.-S. Kim, H.-S. Choi, S. N. Inamdar and J.-S. Yu, *Langmuir*, 2014, **30**, 318–324.

50 W. Deng, Y. Zhang, L. Yang, Y. Tan, M. Ma and Q. Xie, *RSC Adv.*, 2015, **5**, 13046–13051.

51 W. Si, J. Zhou, S. Zhang, S. Li, W. Xing and S. Zhuo, *Electrochim. Acta*, 2013, **107**, 397–405.

52 X. Li, Y. Fang, L. Wen, F. Li, G. Yin, W. Chen, X. An, J. Jin and J. Ma, *Dalton Trans.*, 2016, **45**, 5575–5582.

53 J. Liu, H. Xia, L. Lu and D. Xue, *J. Mater. Chem.*, 2010, **20**, 1506–1510.

54 C. Cheng, G. Zhou, J. Du, H. Zhang, D. Guo, Q. Li, W. Wei and L. Chen, *New J. Chem.*, 2014, **38**, 2250–2253.

55 X. Chi, L. Chang, D. Xie, J. Zhang and G. Du, *Mater. Lett.*, 2013, **106**, 178–181.

56 X. Leng, S. Wei, Z. Jiang, J. Lian, G. Wang and Q. Jiang, *Sci. Rep.*, 2015, **5**, 16629.

57 H.-H. Li, L. Zhou, L.-L. Zhang, C.-Y. Fan, H.-H. Fan, X.-L. Wu, H.-Z. Sun and J.-P. Zhang, *ACS Energy Lett.*, 2017, **2**, 52–59.

58 Z. Fang, W. Xu, T. Huang, M. Li, W. Wang, Y. Liu, C. Mao, F. Meng, M. Wang, M. Cheng, A. Yu and X. Guo, *Mater. Res. Bull.*, 2013, **48**, 4419–4423.

59 Z. Zhang, L. Li, Q. Xu and B. Cao, *RSC Adv.*, 2015, **5**, 61631–61638.

60 J. Mujtaba, H. Sun, G. Huang, K. Mølhave, Y. Liu, Y. Zhao, X. Wang, S. Xu and J. Zhu, *Sci. Rep.*, 2016, **6**, 20592.

61 Y. Bai, X. Wang, X. Zhang, H. Shu, X. Yang, B. Hu, Q. Wei, H. Wu and Y. Song, *Electrochim. Acta*, 2013, **109**, 355–364.

62 A. Y. Shenouda and H. K. Liu, *J. Power Sources*, 2008, **185**, 1386–1391.